

Improved Heavy Dark Matter Annihilation Search from Dwarf Galaxies with HAWC.

The High Altitude Water Cherenkov (HAWC) Collaboration



A. Albert¹ R. Alfaro² C. Alvarez³ A. Andrés⁴ E. Anita-Rangel⁴
M. Araya⁵ J.C. Arteaga-Velázquez⁶ D. Avila Rojas⁴ H.A. Ayala
Solares⁷ R. Babu⁸ P. Bangale⁷ E. Belmont-Moreno² A. Bernal⁴
K.S. Caballero-Mora³ T. Capistrán⁴ A. Carramiñana⁹ F. Carreón⁴
S. Casanova¹⁰ A.L. Colmenero-Cesar⁶ U. Cotti⁶ J. Cotzomi¹¹
S. Coutiño de León³⁰ E. De la Fuente¹³ P. Desiati¹² N. Di Lalla¹⁴
R. Diaz Hernandez⁹ M.A. DuVernois¹² J.C. Díaz-Vélez¹²
K. Engel¹⁵ T. Ergin⁸ C. Espinoza² N. Fraija⁴ S. Fraija⁴
A. Galván-Gámez² J.A. García-González¹⁷ F. Garfias⁴ N. Ghosh¹⁸
A. Gonzalez Muñoz² M.M. González⁴ J.A. González⁶
J.A. Goodman¹⁵ J. Gyeong¹⁹ J.P. Harding¹ S. Hernández-Cadena²⁰
I. Herzog⁸ D. Huang¹⁶ F. Hueyotl-Zahuantitla³ P. Hüntemeyer¹⁸
A. Iriarte⁴ S. Kaufmann²¹ D. Kieda²² K. Leavitt¹⁸ W.H. Lee⁴
J. Lee²³ H. León Vargas² J.T. Linnemann⁸ A.L. Longinotti⁴
G. Luis-Raya²¹ C. Lundy^{8,*} K. Malone¹ O. Martinez¹¹
J. Martínez-Castro²⁴ H. Martínez-Huerta^{16EM} J.A. Matthews²⁵
P. Miranda-Romagnoli²⁶ P.E. Mirón-Enriquez⁴ J.A. Morales-Soto⁶
E. Moreno¹¹ M. Mostafá⁷ M. Najafi¹⁸ A. Nayerhoda¹⁰ L. Nellen²⁷
M.U. Nisa⁸ R. Noriega-Papaqui²⁶ N. Omodei¹⁴ E. Ponce¹¹
Y. Pérez Araujo² E.G. Pérez-Pérez²¹ C.D. Rho¹⁹ A. Rodriguez
Parra⁶ D. Rosa-González⁹ M. Roth¹ H. Salazar¹¹

D. Salazar-Gallegos^{8,*} **A. Sandoval**² **M. Schneider**¹⁵
J. Serna-Franco² **M. Shin**¹⁹ **A.J. Smith**¹⁵ **Y. Son**²³ **R.W. Springer**²²
O. Tibolla²¹ **K. Tollefson**^{8,*} **I. Torres**⁹ **R. Torres-Escobedo**²⁰
F. Ureña-Mena⁹ **E. Varela**¹¹ **L. Villaseñor**¹¹ **X. Wang**²⁸ **Z. Wang**²⁸
I.J. Watson²³ **H. Wu**¹² **S. Yu**²⁹ **X. Zhang**¹⁰ **H. Zhou**²⁰ **C. de León**⁶

¹Los Alamos National Laboratory, Los Alamos, NM, USA

²Instituto de Física, Universidad Nacional Autónoma de México, Ciudad de Mexico, Mexico

³Universidad Autónoma de Chiapas, Tuxtla Gutiérrez, Chiapas, México

⁴Instituto de Astronomía, Universidad Nacional Autónoma de México, Ciudad de Mexico, Mexico

⁵Universidad de Costa Rica, San José 2060, Costa Rica

⁶Universidad Michoacana de San Nicolás de Hidalgo, Morelia, Mexico

⁷ University, Department of Physics, 1925 N. 12th Street, Philadelphia, PA 19122, USA

⁸Department of Physics and Astronomy, Michigan State University, East Lansing, MI, USA

⁹Instituto Nacional de Astrofísica, Óptica y Electrónica, Puebla, Mexico

¹⁰Institute of Nuclear Physics Polish Academy of Sciences, PL-31342 10, Krakow, Poland

¹¹Facultad de Ciencias Físico Matemáticas, Benemérita Universidad Autónoma de Puebla, Puebla, Mexico

¹²Dept. of Physics and Wisconsin IceCube Particle Astrophysics Center, University of Wisconsin—Madison, Madison, WI, USA

¹³Departamento de Física, Centro Universitario de Ciencias Exactas e Ingenierías, Universidad de Guadalajara, Guadalajara, Mexico

¹⁴Department of Physics, 14 University: 14, CA 94305-4060, USA

¹⁵Department of Physics, University of Maryland, College Park, MD, USA

¹⁶Department of Physics and Astronomy, University of Delaware, Newark, DE, USA

¹⁷Tecnológico de Monterrey, Escuela de Ingeniería y Ciencias, Ave. Eugenio Garza Sada 2501, Monterrey, N.L., Mexico, 64849

¹⁸Department of Physics, Michigan Technological University, Houghton, MI, USA

¹⁹Department of Physics, Sungkyunkwan University, Suwon 16419, South Korea

²⁰Tsung-Dao Lee Institute & School of Physics and Astronomy, Shanghai Jiao Tong University, 800 Dongchuan Rd, Shanghai, SH 200240, China

²¹Universidad Politécnica de Pachuca, Pachuca, Hgo, Mexico

²²Department of Physics and Astronomy, University of Utah, Salt Lake City, UT, USA

²³University of Seoul, Seoul, Rep. of Korea

²⁴Centro de Investigación en Computación, Instituto Politécnico Nacional, México City, México.

²⁵Dept of Physics and Astronomy, University of New Mexico, Albuquerque, NM, USA

²⁶Universidad Autónoma del Estado de Hidalgo, Pachuca, Mexico

²⁷Instituto de Ciencias Nucleares, Universidad Nacional Autónoma de Mexico, Ciudad de Mexico, Mexico

²⁸Department of Physics, Missouri University of Science and Technology, Rolla, MO, US

²⁹Department of Physics, Pennsylvania State University, University Park, PA, USA

³⁰Instituto de Física Corpuscular, CSIC, Universitat de València, E-46980, Paterna, Valencia, Spain

*Corresponding authors

E-mail: hawc-publications@umdgrb.umd.edu, salaza82@msu.edu,
claire.lundy@tufts.edu, tollefs2@msu.edu

Abstract. Understanding dark matter’s elusive nature is crucial for the framework of particle physics and expanding the Standard Model. This analysis utilizes the High Altitude Water Cherenkov (HAWC) gamma ray Observatory to indirectly search for dark matter (DM) by studying gamma ray emission from dwarf spheroidal galaxies (dSphs). Selected for their high ratio of dark matter to baryonic matter, dSphs are useful for this type of search owing to the low background emission. In comparison to previous HAWC studies, we significantly improve our sensitivity to DM from dSphs due to improvements to our event reconstruction and reduced hadronic contamination. We expanded the number of dSphs studied, DM annihilation channels into the Standard Model (SM), and the amount of data collected on each previously studied dSph. We searched for DM signals in each dSph using the latest version of the algorithms used to reconstruct data from the primary detector of the HAWC instrument. We report that we do not detect evidence of DM from dSphs, so we place upper limits for the velocity-weighted DM annihilation cross-section ($\langle\sigma v\rangle$) on the order of $10^{-23} \text{ cm}^3\text{s}^{-1}$ for a DM mass range of $1 - 10^4 \text{ TeV}$.

Contents

1	Introduction	1
2	The HAWC Observatory	2
3	Background	3
4	Analysis	3
4.1	DM to gamma ray Spectra	4
4.1.1	Inverse Compton Scattering	5
4.2	Dark Matter Density Distributions and Source Selection	5
4.2.1	\mathcal{LS} Catalog	6
4.2.2	\mathcal{GS} Catalog	7
4.3	Systematics	7
5	Results	8
6	Conclusion and Discussion	15
A	Likelihood Methods	20
B	Remaining Spectra Models	21
C	Differential J-factor as a Function of θ	22

1 Introduction

While evidence for the existence of dark matter (DM) has been observed clearly within the universe, its true nature is yet to be uncovered. The large rotational velocities of galaxies compared to their visible mass content [1] is just one piece of evidence for DM’s existence. There are numerous particle candidates that could potentially make up all or a fraction of DM [1]. To narrow our search and discuss more specific candidates, we assume a Cold Dark Matter (CDM) structure formation history. This defines dark matter as non-relativistic, or “cold”. Within these constraints, there is motivation for the so-called Weakly Interacting Massive Particles (WIMPs) as a potential dark matter candidate. WIMPs interact only through the weak and gravitational forces and exist at mass scales from GeV to TeV [2]. In this study, we presume heavy WIMP DM can annihilate into Standard Model (SM) particles which decay to final state photons that HAWC can detect.

Our search focuses solely on dwarf spheroidal (dSphs) galaxies. These make ideal targets for a DM search because of their high dark matter to baryonic matter ratio, low overall baryonic matter content, and position as satellites of the Milky Way [3]. We selected 17 dSphs for this analysis due to their positions in HAWC’s field of view (FOV) from about -26° to $+64^\circ$ [4] and well-studied dark matter parameters. Previous HAWC studies were limited to 15 dSphs [5] because observations of Willman 1 and Draco II had significant uncertainties [6]. Recent observations [7, 8] constrain the DM densities around these two dSphs, so we include them for this study. The dSphs considered in this analysis are Boötes I, Canes Venatici I,

Canes Venatici II, Coma Berenices, Draco, Draco II, Hercules, Leo I, Leo II, Leo IV, Leo V, Pisces II, Segue 1, Sextans, Ursa Major I, Ursa Major II, and Willman 1. The properties of these sources are listed in Tab. 1.

This work is built off previous HAWC analyses [5, 9, 10], and this study improves on the previous in the following ways. The particle physics model used for gamma ray spectra was updated to incorporate recent measurements and constraints in particle physics. The details of this are discussed in Sec. 4.1. For this study, HAWC samples DM masses up to 10 PeV, where previously we stopped at 1 PeV [10]. To model the DM spatial profiles, we use two different DM density publications: from A. Pace and L. Strigari [7] and Geringer-Sameth [8].

We also implement significant updates to HAWC’s data and reconstruction that improved on our energy estimation and gamma/hadron separation. Unlike previous HAWC dSphs analyses that relied on an older “Pass 4” reconstruction [5, 10, 11] and used the fraction of the PMT hits on the main array (f_{hit}) [9], we utilize the newer “Pass 5” reconstructed data [12] that significantly improves on HAWC’s angular resolution and sensitivity. We also use a Neural Network (NN) based energy estimator, improving on the energy resolution and the maximum energy sensitivity in this work. Additionally, HAWC introduced a Machine Learning (ML) optimization suite for selecting cuts on event data in the detector that better discriminates between gamma rays versus hadrons [13]. These newer datasets improve our sensitivity by more precisely estimating the energies of photon events and reducing the cosmic ray contamination in the gamma ray data.

In this paper, we construct spatial models for the dark matter content of each dSph and annihilation spectra for 17 SM channels to calculate the expected gamma ray flux due to dark matter annihilation. Section 3 describes the HAWC observatory and our method of background estimation. Section 4 details our method of determining DM annihilation using the DM density calculated from two different dSph catalogs and gamma ray spectra. Section 5 contains the results of our analysis across both catalogs of 17 dwarfs for each SM channel. While no gamma ray excess was found in the dSphs, we present the upper limits on annihilation cross-section for each dSph and SM channel and compare to previous searches and sensitivities. Finally, Sec. 6 contains the conclusion and discussion of our results.

2 The HAWC Observatory

Located near the Sierra Negra volcano in Puebla, Mexico, the High-Altitude Water Cherenkov (HAWC) Observatory detects high-energy gamma rays and cosmic rays. Its main array has been operating since March 2015 with an uptime of over 95%. HAWC is positioned at 4,100 meters above sea level and covers over 100,000 m² [4]. Its FOV captures a declination range from about -26° to +64° [4]. HAWC is composed of a number of water Cherenkov detectors (WCDs) that are separated into a main array and outriggers. The main array covers an area of 22,000 m² and is composed of 300 WCDs, each equipped with 200 kL of purified water and 4 photomultiplier tubes (PMTs) to detect charged particle showers from cosmic- or gamma rays of energies from 0.1 TeV to over 100 TeV [14]. Outside the main array are the outriggers. These cover an area of 100,000 m² and are 350 smaller WCDs containing only 1 PMT each and spaced much farther apart. These provide additional resolution to air showers whose cores fall outside the main array by improving our overall angular reconstruction and energy estimation [14].

When a very high-energy gamma ray enters Earth’s atmosphere, it interacts with the atmospheric particles and causes an extensive air shower. The showers are composed of

secondary particles that "rain" down on Earth. When the charged particles enter into the WCDs they produce Cherenkov light detected by the PMTs. HAWC records the time and charge measured by the PMTs [4]. We estimate the energy, reconstruct the direction of the primary particle, and discriminate between cosmic and gamma rays from the ensemble of PMT hit data [11]. These events are sorted into analysis bins developed using a NN energy reconstruction algorithm as described in [13, 15].

The gamma ray dataset used in this study includes 3070 days of HAWC operation, compared to 507 days from [5], and 1038 days from [9] and [10]. This study also utilizes events which have reconstructed shower cores off the main and implements highly sensitive cuts discerned with ML algorithms [13], neither of which has been done in previous DM dSph studies. In our analysis framework, we used HAWC public likelihood fitting software HAL and `threeML` [16]. dSphs are treated as extended sources in HAWC data and are analyzed as described in [5].

3 Background

We consider the following for estimating the background around dSphs. The dSphs' angular extent are similar to HAWC's spatial resolution, so the analysis is not contaminated by large-scale anisotropies in the cosmic ray background. Most sources are fully contained within 1-5 `HEALpix` pixels with only a couple (Sextans and Ursa Major II) dSphs requiring more, with a pixel size of 0.025 steradians. The dSphs used in this analysis are off the galactic plane and therefore not contaminated by diffuse emission from the Milky Way. Moreover, they are baryonically faint relative to their expected dark matter content and do not host bright high-energy gamma ray sources. Therefore, we make no additional assumptions on the background from our sources and use HAWC's standard direct integration method for low energy, gamma ray background estimation [11, 17], and background randomization [15] for the highest energy gamma rays.

The largest background under this consideration is from an isotropic flux of cosmic rays. The contamination of this hadronic flux is worse at lower energies where HAWC's gamma ray and hadronic events appear identical.

4 Analysis

The expected differential photon flux from DM-DM annihilation to standard model particles is described as

$$\frac{d\Phi_\gamma}{dE_\gamma} = \frac{\langle\sigma v\rangle}{8\pi m_\chi^2} \frac{dN_\gamma}{dE_\gamma} \times J, \quad (4.1)$$

where $\langle\sigma v\rangle$ is the velocity weighted annihilation cross-section, $\frac{dN}{dE}$ is the expected energy-weighted differential number of photons produced at annihilation, m_χ is the rest mass of the supposed DM particle, and J is the astrophysical J -factor, integrated over a solid angle, Ω . J is defined as

$$J = \int d\Omega \int_{l.o.s} dl \rho_\chi^2(r, \theta'), \quad (4.2)$$

where ρ_χ is the DM density, l is the line of sight distance to the source from Earth, r is the radial distance from the center of the source, and θ' is the half angle defining a cone

containing the DM source. How each component is synthesized and considered for HAWC’s analysis is presented in the following sections. Section 4.1 presents the particle physics model for DM annihilation. Section 4.2 presents the spatial distributions built for each dSph.

4.1 DM to gamma ray Spectra

We use `HDMSpectra` (HDMS) [18] for the estimation of the gamma ray spectra for each DM annihilation channel to the SM. This repository is comparable to the *Poor Particle Physicist Cookbook* (PPPC) for Dark Matter Indirect Detection [19] DM spectral models but includes electro-weak (EW) corrections and higher-order loop corrections from W and Z bosons [18]. These corrections allow for production of photon spectra from the EW to Planck scale, making it ideal for our mass range of heavy DM.

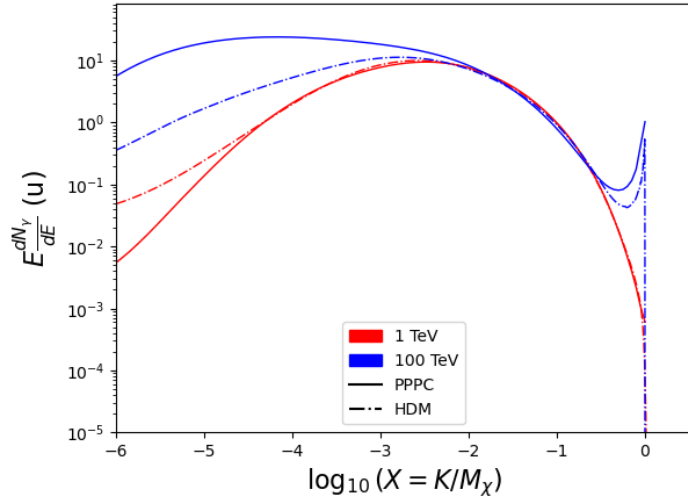


Figure 1. Spectral hypotheses from PPPC and HDMS for DM annihilation: $\chi\chi \rightarrow W^-W^+$. The x-axis is the \log_{10} of X , where X is the ratio of gamma ray energy to DM mass. The y-axis is the unitless, energy-weighted gamma ray counts. Solid lines are spectral models with EW corrections from the PPPC. Dash-dot lines are spectral models from HDMS. Red lines are models for $M_\chi = 1$ TeV, the lowest in our studied range. Blue lines represent models for $M_\chi = 100$ TeV, which are well above PYTHIA’s limits, where corrections are necessary [18].

Figure 1 demonstrates the impact of changes implemented with HDMS on DM annihilation to W bosons in contrast to the PPPC. At masses around 1 TeV, the spectra fall in general agreement while at masses of 100 TeV, the HDMS spectrum initially falls an order of magnitude below the PPPC line and maintains a more conservative model. The SM DM annihilation channels studied here are $\chi\chi \rightarrow: e^+e^-, \mu^+\mu^-, \tau^+\tau^-, b\bar{b}, t\bar{t}, W^+W^-, Z^0Z^0, u\bar{u}, d\bar{d}, \nu_e\bar{\nu}_e$, and $\gamma\gamma$.

For the $\gamma\gamma$, W^+W^- , and Z^0Z^0 annihilation channels, a substantial fraction of the signal photons are expected to have $E_\gamma \approx m_\chi$ [18]. This introduces a spectral line that is much narrower than the energy resolution of the HAWC detector. To ensure that we do not underestimate the gamma ray contribution to the flux, the line feature is convolved with a Gaussian kernel with a 1σ on-sided width of 5% m_χ and total convolution window of $\pm 4\sigma$. The kernel width was chosen based on the energy resolution of the utilized energy estimator (similar to [10]). The NN energy estimator’s (see [20]) improved energy resolution compared to f_{hit} , an alternative method of binning data by fraction of PMTs hit [11], at low gamma ray

energy enables narrower kernels. This kernel is not well represented at lower photon energies and underestimates the photon spectra, but agrees at high energies. Ultimately, because our analysis is focused on constraining the upper end of the mass range, this approximation is adequate for our purposes. The annihilation spectra after Gaussian smoothing for $\chi\chi \rightarrow \gamma\gamma$, W^+W^- , and Z^0Z^0 spectral hypotheses are shown in Fig. 2.

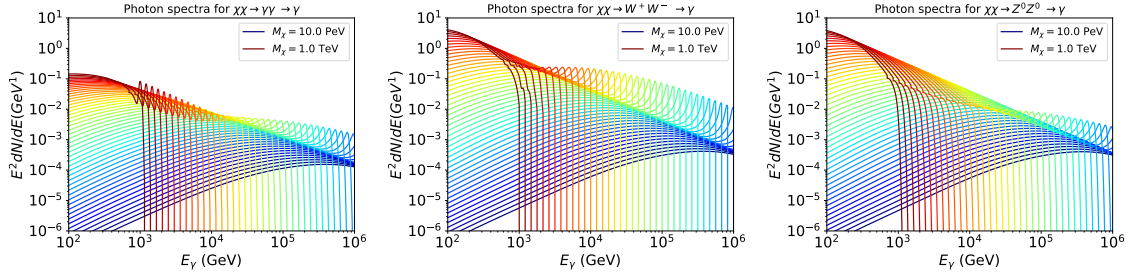


Figure 2. Photon spectra for $\chi\chi \rightarrow \gamma\gamma$ (left), $\chi\chi \rightarrow WW$ (middle), and $\chi\chi \rightarrow Z^0Z^0$ (right) after Gaussian convolution of line features. Both the 1 TeV and 10 PeV spectra have δ -line features at $E_\gamma = m_\chi$. Redder lines are annihilation spectra with lower DM mass. Bluer lines are spectra from larger DM mass. All spectral models are sourced from the `HDMSpectra` (HDMS) models [18]. Axes are drawn according to the energy sensitivity of HAWC.

4.1.1 Inverse Compton Scattering

One effect previously not considered was signal enhancement in the photon spectra due to the electron final state process: $\chi\chi \rightarrow \text{SM SM} \rightarrow e^\pm$. It is expected that all DM annihilation channels will produce high energy electrons which should radiate high energy gamma rays via Inverse Compton Scattering (ICS). The enhancement of the gamma ray spectra will depend on the electron and light bath of the electrons in transit to Earth and initial energy distribution of the electrons. We use the tools provided by the PPPC [19] for calculating the impact of ICS for a given location in the sky and annihilation channel. We studied the enhancement of the gamma ray spectra due to ICS for the e^+e^- channel only, as it would produce the largest number of high energy electrons. Additionally, we check this enhancement for two dwarfs (Segue 1 and Coma Berenices) with high J -factors which contribute substantially to the combined limits. Using the tools provided by the PPPC on ICS [19] the enhancement from ICS for both dwarves was negligible compared to the primary photon spectra. Therefore, it was not considered to significantly impact our study.

No adjustments were made to the spectral models for the remaining annihilation channels, which are plotted for each m_χ in Sec. B.

4.2 Dark Matter Density Distributions and Source Selection

J -factors are the largest source of model uncertainty in our analysis. The J -factor spatial templates for each source are created using the scale radius and scale density parameters of each dSph (see Eqs. (4.2) and (4.3)) with a region of interest of 4° centered on each dSph. Because the angular size of the dSphs are close to HAWC’s angular resolution, we are not as sensitive to the underlying DM density distribution. We are, however, sensitive to the stellar selection and statistical priors that inform the J -factor fit. Therefore, we selected studies with diverse methods of deriving J -factors (see Sections 4.2.1 and 4.2.2). We implement dSph DM density parameters from both Louis Strigari et al. (referred to with \mathcal{LS}) [7] and

Alex Geringer-Sameth et al. (referred to with \mathcal{GS}) [8]. The parameters used for this study are summarized in Tab. 1.

Name	\mathcal{LS} Distance (kpc)	\mathcal{GS} Distance (kpc)	l, b (°)	α_c (°)	$\log_{10} J$ (\mathcal{LS} set) $\log_{10}(\text{GeV}^2\text{cm}^{-5}\text{sr})$	$\log_{10} J$ (\mathcal{GS} set) $\log_{10}(\text{GeV}^2\text{cm}^{-5}\text{sr})$
Boötes I	66.0 ± 3.0	66.0	358.08, 69.62	0.325	$17.83^{+0.44}_{-0.45}$	$17.79^{+0.23}_{-0.25}$
Canes Venatici I	210.0 ± 6.0	218.0	91.39, 73.24	0.231	$17.24^{+0.36}_{-0.34}$	$17.38^{+0.12}_{-0.11}$
Canes Venatici II	160.0 ± 7.0	160.0	113.58, 82.70	0.049	$17.43^{+0.61}_{-0.62}$	$17.20^{+0.40}_{-0.44}$
Coma Berenices	42.0 ± 1.5	44.0	241.89, 83.61	0.156	$18.67^{+0.36}_{-0.35}$	$18.39^{+0.30}_{-0.33}$
Draco	76.0 ± 6.0	76.0	86.37, -34.72	0.274	$18.80^{+0.26}_{-0.25}$	$18.75^{+0.20}_{-0.21}$
Draco II	20.0 ± 3.0	20.0	98.29, 42.88	0.069	$19.43^{+0.98}_{-1.35}$	$18.31^{+0.60}_{-0.72}$
Hercules	132.0 ± 6.0	132.0	28.73, 36.87	0.085	$17.12^{+0.71}_{-0.71}$	$16.94^{+0.33}_{-0.38}$
Leo I	258.2 ± 9.5	254.0	226.00, 49.10	0.130	$17.51^{+0.31}_{-0.31}$	$17.74^{+0.09}_{-0.09}$
Leo II	233.0 ± 15.0	233.0	220.17, 67.23	0.078	$17.53^{+0.30}_{-0.30}$	$17.59^{+0.11}_{-0.11}$
Leo IV	154.0 ± 5.0	154.0	265.44, 56.51	0.083	$16.69^{+0.95}_{-1.41}$	$16.59^{+0.52}_{-0.64}$
Leo V	173.0 ± 5.0	178.0	261.86, 58.54	0.020	$17.79^{+0.91}_{-0.76}$	$16.58^{+0.62}_{-0.70}$
Pisces II	183.0 ± 15.0	182.0	79.21, -47.11	0.030	$17.50^{+1.06}_{-1.06}$	$16.57^{+0.65}_{-0.77}$
Segue 1	23.0 ± 2.0	23.0	220.50, 50.40	0.105	$18.90^{+0.58}_{-0.62}$	$18.91^{+0.39}_{-0.45}$
Sextans	92.5 ± 2.2	86.0	243.50, 42.27	0.648	$17.74^{+0.33}_{-0.33}$	$18.32^{+0.23}_{-0.23}$
Ursa Major I	97.3 ± 5.85	97.0	159.40, 54.40	0.234	$18.16^{+0.47}_{-0.45}$	$18.18^{+0.22}_{-0.25}$
Ursa Major II	34.7 ± 2.1	32.0	152.50, 37.40	0.327	$19.34^{+0.59}_{-0.61}$	$18.78^{+0.36}_{-0.42}$
Willman 1	38.0 ± 7.0	38.0	158.58, 56.78	0.054	$19.18^{+0.41}_{-0.35}$	$18.02^{+0.59}_{-0.69}$

Table 1. Summary of the relevant properties of the dSphs used in the present work. Columns 2 and 3 present their heliocentric distances as reported by \mathcal{LS} and \mathcal{GS} , respectively, where uncertainties are included when reported. Column 4 is the galactic coordinates of each dwarf. Column 5 is $\alpha_c = 2r_{1/2}/d$, the profile cut off angle where \mathcal{LS} J-factor uncertainties are minimized [7]. Columns 6 and 7 give the J-factors of each source from the \mathcal{LS} and \mathcal{GS} studies, respectively, and estimated $\pm 1\sigma$ uncertainties. The values $\log_{10} J$ (\mathcal{LS} set) [7] correspond to the mean J-factor values for a source extension truncated at α_c while the values $\log_{10} J$ (\mathcal{GS} set) [8] correspond to the median J-factor values for a source extension truncated at 0.5° .

Both catalogs fit a Navarro–Frenk–White (NFW) [21] spatial DM distribution to the dSphs which has a DM density of

$$\rho(r) = \frac{\rho_0}{\frac{r}{R_s} \left(1 + \frac{r}{R_s}\right)^2}. \quad (4.3)$$

The scale density, ρ_0 , and the scale radius, R_s are free parameters fit for each dSph in the \mathcal{LS} and \mathcal{GS} catalogs. r is the distance from the center of the dSph. Using these reported parameters, we extract median and $\pm 1\sigma$ J-factor distributions for each dwarf. Section C includes figures of both the median and $\pm 1\sigma$ for the $\frac{dJ}{d\Omega}$ values as functions of θ . The differences in catalogs are discussed in the following two sections.

4.2.1 \mathcal{LS} Catalog

The \mathcal{LS} catalog determines the parameters for 43 dwarfs through log-uniform priors. This publication postulates that because the J-factor can be thought of as a “flux”, it will scale as the inverse of distance squared. They further develop a scaling relation of the form

$$J_{\text{model}}(\theta_{\text{max}}) = J_0 \left(\frac{\sigma_{\text{los}}}{5 \text{ km s}^{-1}} \right)^{\gamma_{\sigma_{\text{los}}}} \left(\frac{d}{100 \text{ kpc}} \right)^{\gamma_d} \left(\frac{r_{1/2}}{100 \text{ pc}} \right)^{\gamma_{r_{1/2}}} \quad (4.4)$$

to model the J -factor as a function of the kinematic parameters of the dwarf where σ_{los} is the line-of-sight velocity dispersion, d is the heliocentric distance, $r_{1/2}$ is the half-light radius, and $\gamma_{\sigma_{\text{los}}} = 4$, $\gamma_d = -2$, and $\gamma_{r_{1/2}} = -1$ are fixed slope parameters. The uncertainty of this J -factor is minimized at the angle $\alpha_c = 2r_{1/2}/d$ [7].

The 2D maps used as input for HAWC analysis were constructed using the `Gammapy` Python package [22]. The dwarf parameters can be used to determine the scale radius $r_s = 4r_{1/2}$ and the scale density

$$\rho_s r_s = \frac{5\sigma_{\text{los}}^2 r_{1/2}}{2G} \frac{1}{4\pi r_s^2 \mathbf{g}(\mathbf{r}_{1/2}/\mathbf{r}_s)}, \quad (4.5)$$

where $\mathbf{g}(\mathbf{x}) = \log(1+x) - x/(1+x)$. Spatial templates in $\frac{dJ}{d\Omega}(\theta)$ up to an angular separation of α_c were created to minimize J -factor uncertainties [7].

4.2.2 \mathcal{GS} Catalog

The \mathcal{GS} catalog is an important addition to this analysis because it provides kinematic priors for dSphs rather than just cosmological log-uniform priors as in [7]. \mathcal{GS} adopts a WIMP dark matter model rather than maintaining model independence. This is not a problem for our Heavy WIMP search but extremely high mass becomes harder to motivate with this catalog. For classical dwarfs, this change is mostly inconsequential, as their well-defined velocity dispersion profiles allow for an accurate posterior even in the case of log-uniform priors. Yet for ultra-faints, the low statistics benefits from kinematic priors. These new priors ultimately lower the J -factors across the catalog and weaken the dark matter annihilation cross-section limits [8].

This catalog is also constructed using `Gammapy`. The ρ_s and r_s priors are not directly reported, however, and must be generated through Monte Carlo (MC) simulation [8]. \mathcal{GS} reports a third parameter r_t , the tidal truncation radius, which we use to truncate the J -factor distributions. From there, the J -factor can be approximated as described in [23] for each MC sample. We then use the median J -factor to produce the spatial template up to an angular separation of 0.5° .

4.3 Systematics

The largest uncertainties in this analysis are the choices of J -factor model, which has been discussed at length in Sec. 4.2. The second-largest contributor is the systematics from the detector response (DR). We study the impact of detector uncertainties from PMT efficiencies, late light, and calibration epochs. When considering calibration epochs, we model our response for HAWC as early as first light in 2015. Since then, there have been a varying number of PMTs and WCDs online. We studied the effect of these different HAWC snapshots and varied signal acceptance and charge deposition rates via detector simulation [15]. We found the effects of these systematics to fall within our 68% containment band and in most cases only deviating by an average factor of 1.02. In the worst case, a simulation of early HAWC runs differed by a factor of 1.81 in the $\tau^-\tau^+$ channel at a mass of 681 TeV of the \mathcal{LS} catalog, which falls within the 68% containment for this model.

5 Results

17 dSphs common between \mathcal{GS} and \mathcal{LS} are considered for the analysis. These dSphs are analyzed for emission from DM annihilation according to the likelihood method described in Sec. A. The likelihood profiles are then stacked to synthesize a combined limit on the dark matter annihilation cross-section, $\langle\sigma v\rangle$. This combination is done for each of the 11 SM annihilation channels over a mass range from 1 TeV to 10 PeV. The mass range is separated into 25 log-spaced bins for all channels except $\gamma\gamma$ and Z^0Z^0 , which have 49 log-spaced bins. The combined limits for all annihilation channels with HAWC’s observations are shown in Fig. 5 for the \mathcal{LS} catalog and Fig. 6 for the \mathcal{GS} catalog. Test statistics (TS) of the best fit $\langle\sigma v\rangle$ values for each m_χ and SM channel are shown in Fig. 7 for the \mathcal{LS} catalog and Fig. 8 for the \mathcal{GS} catalog. Here, we show updated limits for $\chi\chi \rightarrow b\bar{b}$, $t\bar{t}$, $u\bar{u}$, $d\bar{d}$, W^-W^+ , $\nu_e\bar{\nu}_e$, e^-e^+ , $\mu^-\mu^+$, $\tau^-\tau^+$, $\gamma\gamma$ and Z^0Z^0 . We also simulated 300 studies of Poisson background trials to produce $\pm 1\sigma$ and $\pm 2\sigma$ uncertainty bands. The results of these trials are shown in Fig. 3 for the \mathcal{LS} catalog and in Fig. 4 for the \mathcal{GS} catalog. We see a general tendency of the observed limit to fall in line with the expected limits. This is especially true in the hard channels and even more so in the \mathcal{LS} catalog. The soft channels tend to see slight deviations within the 95% band at the lowest masses. At our middle and high range masses, the observed annihilation cross-section generally falls in line with the expectation in the \mathcal{LS} catalog. In the \mathcal{GS} catalog, we see the observed fall closest to the expected between 10 and 100 TeV.

HAWC reports no evidence for DM in dSphs observations, and sets competitive limits for heavy WIMP DM. We set the most constraining limits on $\chi\chi \rightarrow b\bar{b}$ within the mass range of 30 TeV to 10 PeV. Similarly, we define the constraints on $\chi\chi \rightarrow \tau^+\tau^-$ in the DM mass range between 4 TeV and 1 PeV. Within the \mathcal{LS} catalog, the largest excess found in HAWC data was for DM annihilating to $b\bar{b}$ for $m_\chi = 1$ TeV at a pre-trials significance of 2.17σ . In the \mathcal{GS} catalog, the largest excess found was also for DM annihilating to $b\bar{b}$ for $m_\chi = 1$ TeV at a pre-trials significance of 2.53σ . Across both catalogs, Sextans and Hercules show excesses around $m_\chi = 10$ TeV and $m_\chi = 100$ TeV, respectively. Additionally, Segue 1 maintains its position as one of the strongest contributors to the limits as a single source in both catalogs. This is no surprise as it is a well studied classical dwarf and is located overhead in HAWC’s FOV. Notably, Willman 1 in the \mathcal{LS} catalog plays a large role in defining the upper limits in the high mass ranges. This is due to its large and well-defined J -factor. As expected with lowered J -factors, the \mathcal{GS} catalog shows weakened combined limits in comparison to \mathcal{LS} . Despite this, the utilization of physically motivated priors makes it an important addition to this analysis.

In Fig. 9, this work sets strong limits in high DM regions when compared to other, similar DM searches in dSphs. Both catalogs have extended HAWC’s mass range into the PeV range. Initially, the \mathcal{LS} catalog was included as a point of comparison for the \mathcal{GS} catalog given the amount of changes and improvements were made in comparison to previous HAWC DM searches. It displays strong limits in the high mass ranges when compared to other experiments. The limits from both catalogs provide information on DM annihilation from dSphs in the more general and frequently-used case of log-uniform priors (\mathcal{LS}) and the more specific kinematic priors (\mathcal{GS}).

Finally, we include data on the gamma ray flux as well as the flux upper bounds per energy bin for each source location in Tables 2 and 3 respectively. The gamma flux upper bounds are an important factor in reproducing our $\langle\sigma v\rangle$ limits. HAWC detects mainly cosmic rays, making gamma-hadron separation an integral feature of data analysis. The HAWC

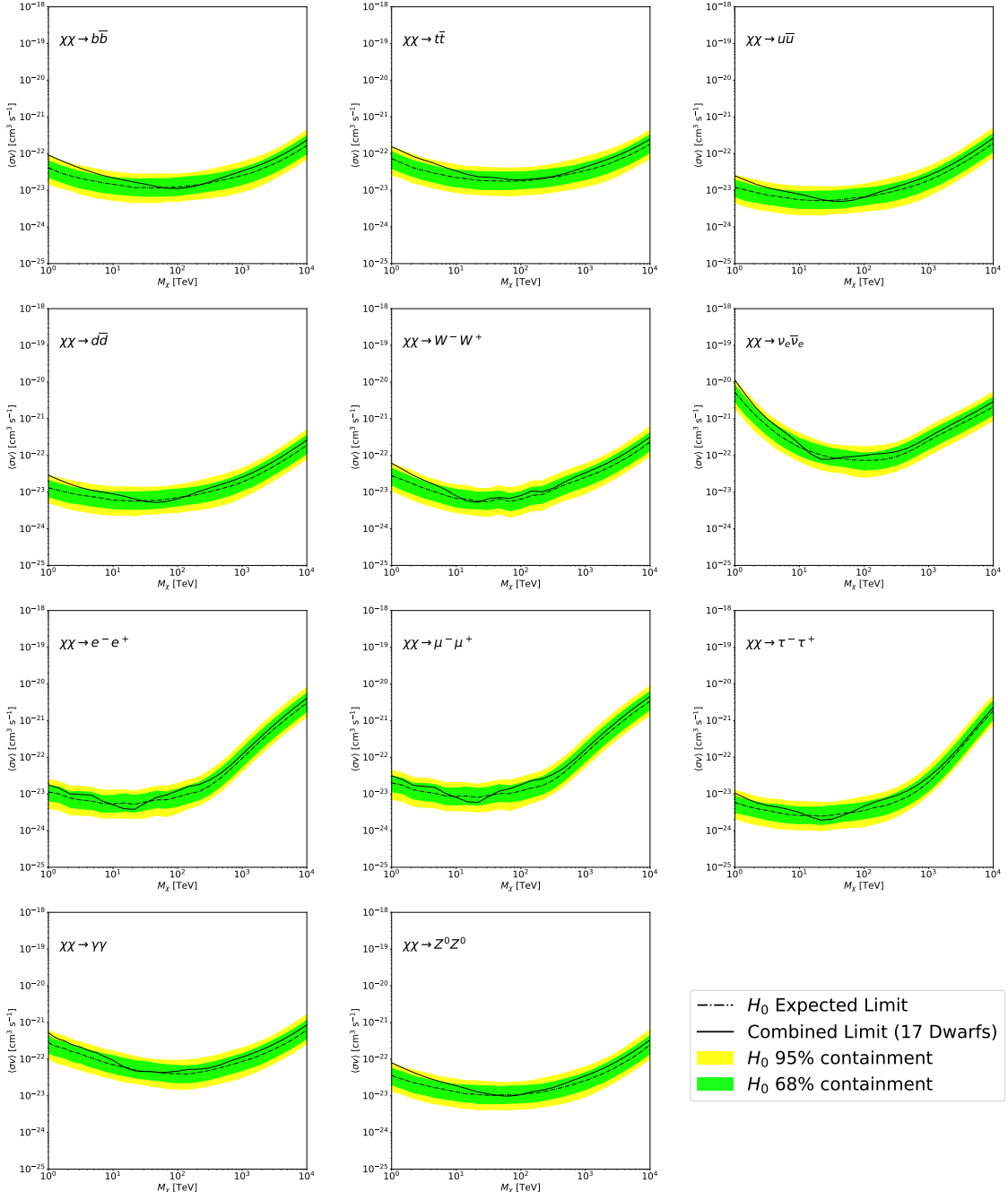


Figure 3. Brazil bands on $\langle\sigma v\rangle$ versus m_χ for $\chi\chi \rightarrow b\bar{b}$, $t\bar{t}$, $u\bar{u}$, $d\bar{d}$, W^-W^+ , $\nu_e\bar{\nu}_e$, e^-e^+ , $\mu^-\mu^+$, $\tau^-\tau^+$, $\gamma\gamma$ and Z^0Z^0 . Limits are with \mathcal{LS} J -factors [7]. The solid line represents the observed combined limit. The dashed line represents the expected annihilation cross-section from HAWC background. The green and yellow bands show 68% and 95% containment respectively.

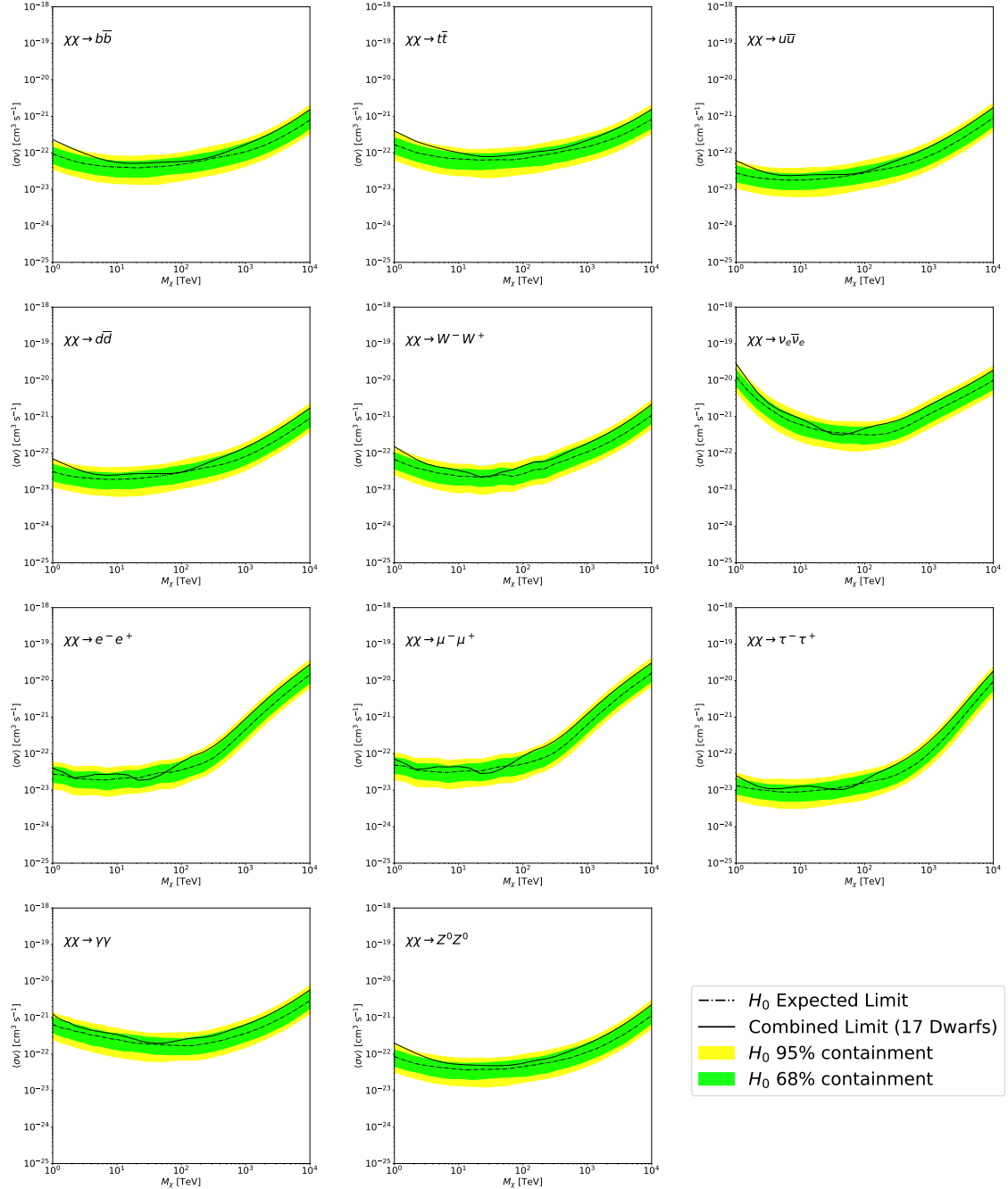


Figure 4. Same as Fig. 3 but with \mathcal{GS} J -factors [8].

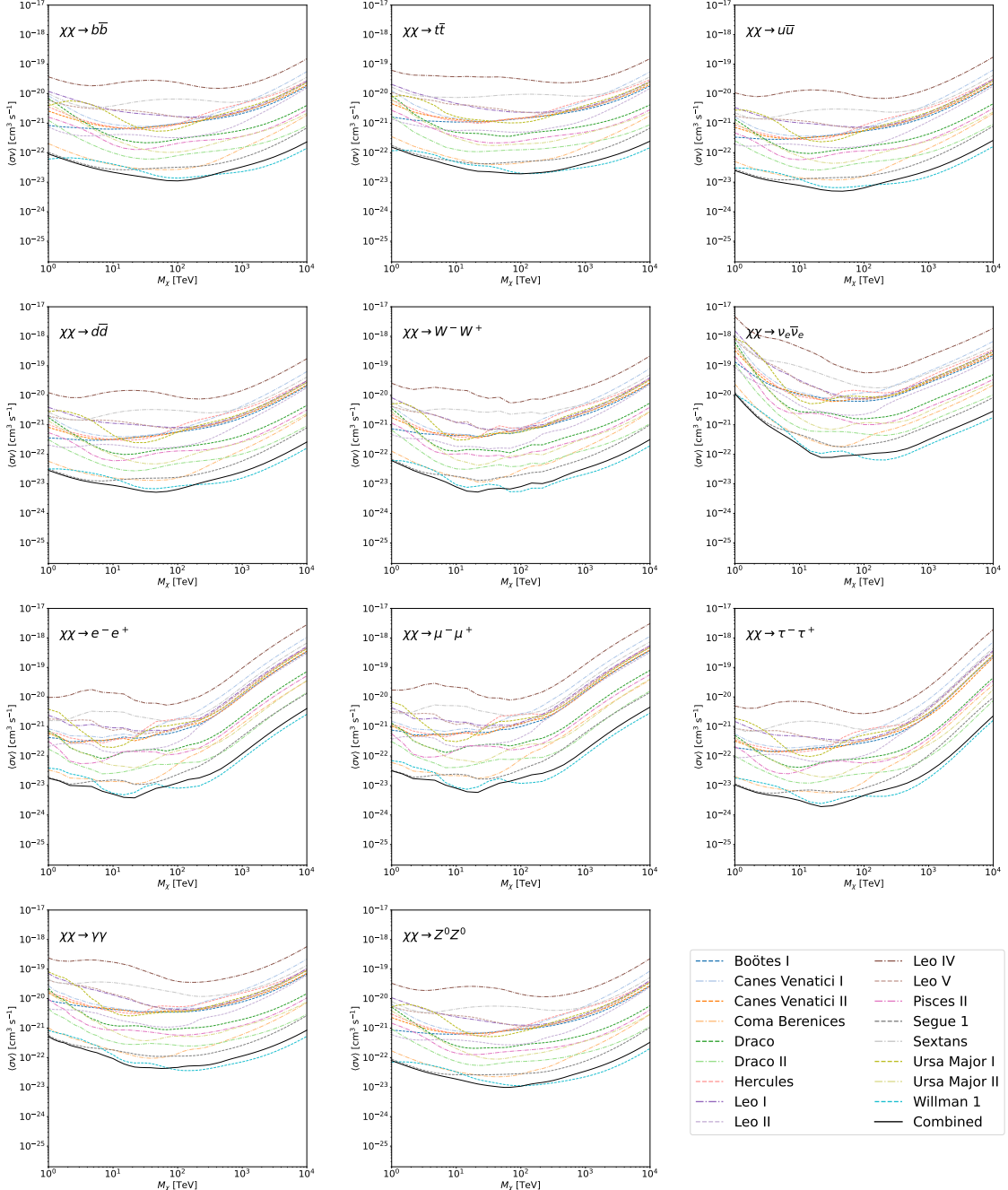


Figure 5. HAWC upper limits at 95% confidence level on $\langle\sigma v\rangle$ versus m_χ for $\chi\chi \rightarrow b\bar{b}$, $t\bar{t}$, $u\bar{u}$, $d\bar{d}$, W^-W^+ , $\nu_e\bar{\nu}_e$, e^-e^+ , $\mu^-\mu^+$, $\tau^-\tau^+$, $\gamma\gamma$ and Z^0Z^0 . Limits are with \mathcal{LS} J -factors [7]. The solid line represents the observed combined limit. Dashed lines represent limits from individual dSphs.

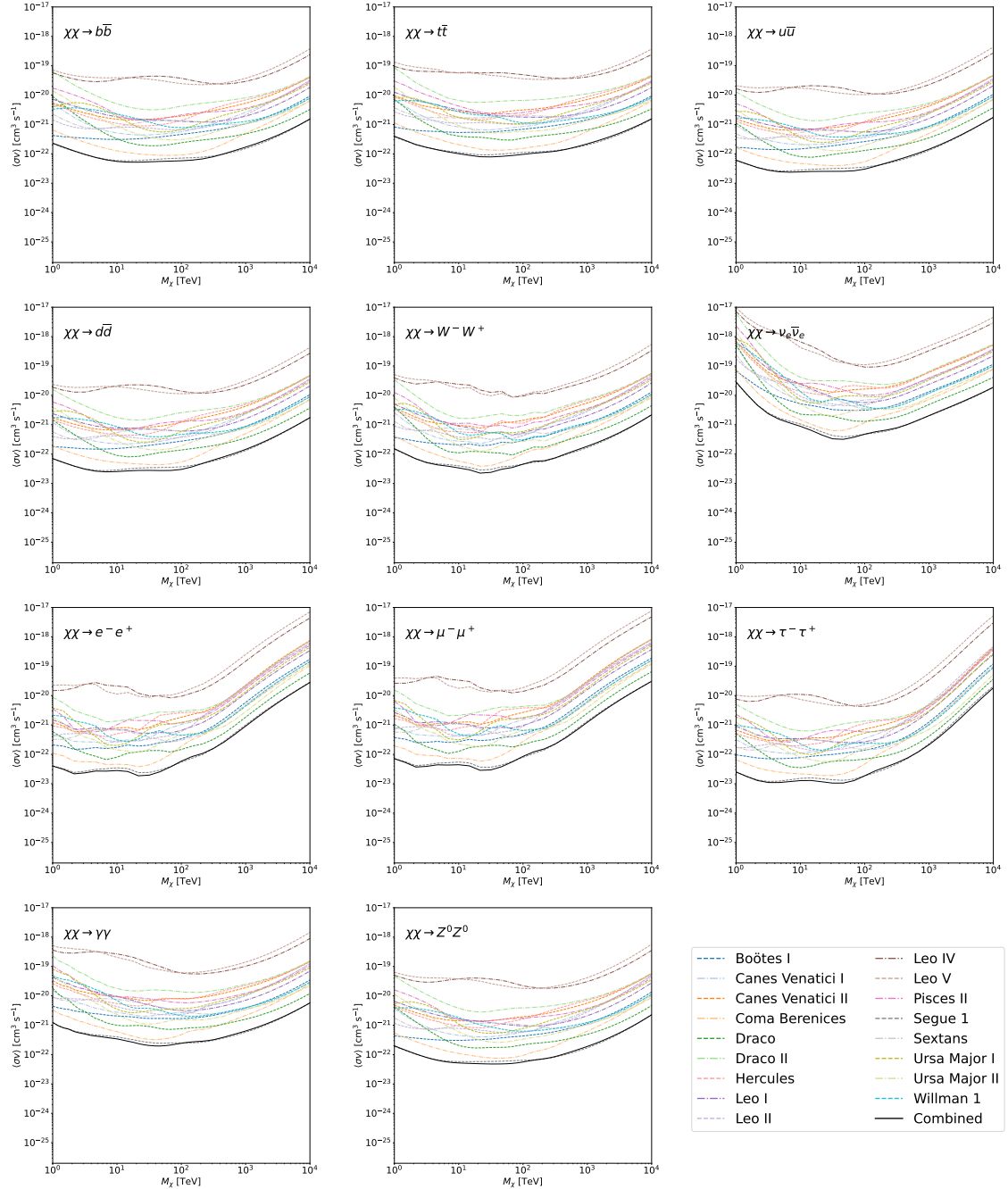


Figure 6. Same as Fig. 5 but with \mathcal{GS} J -factors [8].

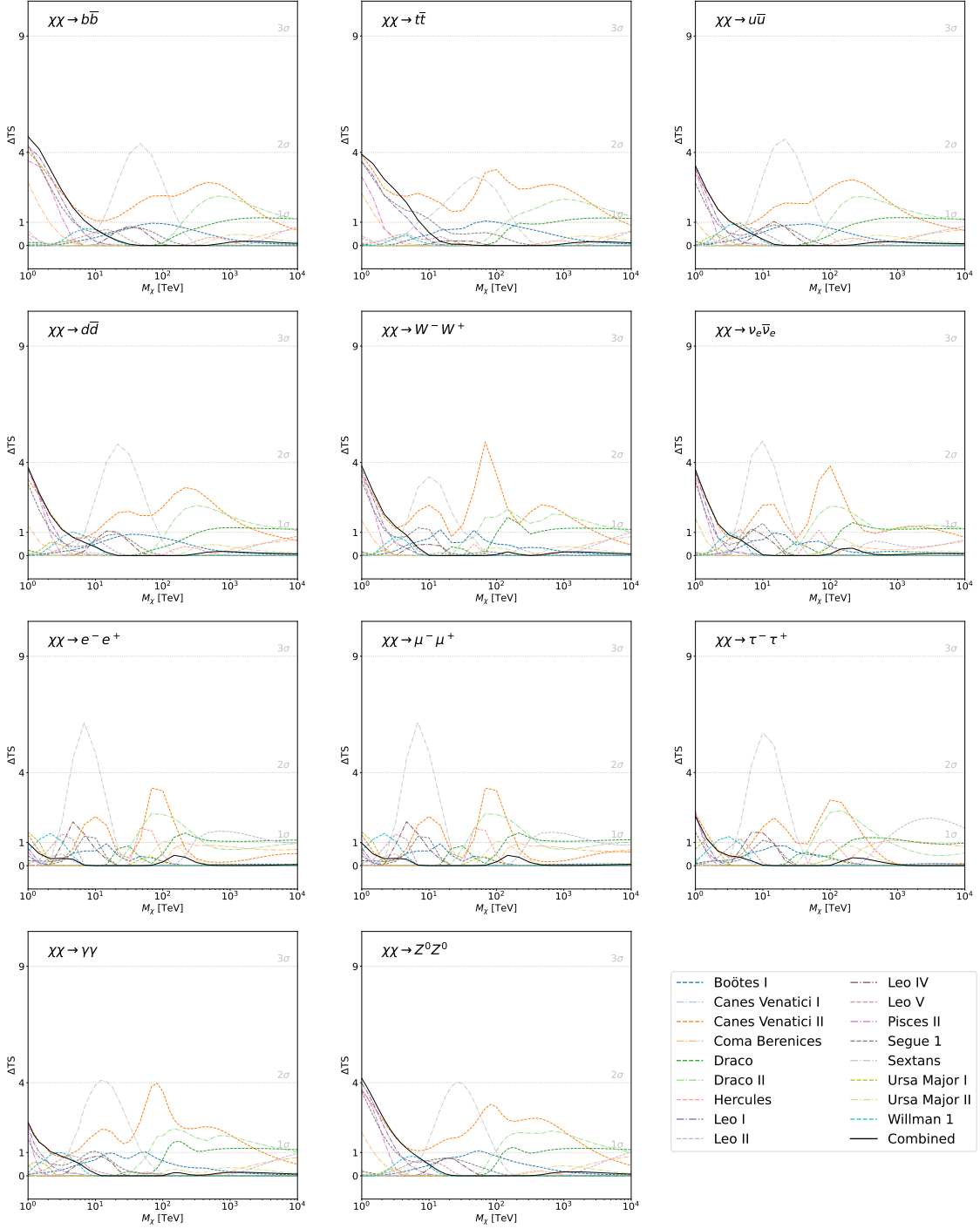


Figure 7. HAWC TS values for best fit $\langle \sigma v \rangle$ versus m_χ for SM annihilation channels: $\chi\chi \rightarrow b\bar{b}$, $t\bar{t}$, $u\bar{u}$, $d\bar{d}$, W^-W^+ , $\nu_e\bar{\nu}_e$, e^-e^+ , $\mu^-\mu^+$, $\tau^-\tau^+$, $\gamma\gamma$ and Z^0Z^0 . Limits use \mathcal{LS} J -factors. The solid black line shows the combined best fit TS values. The colored, dashed lines are the TS values from each dSph.

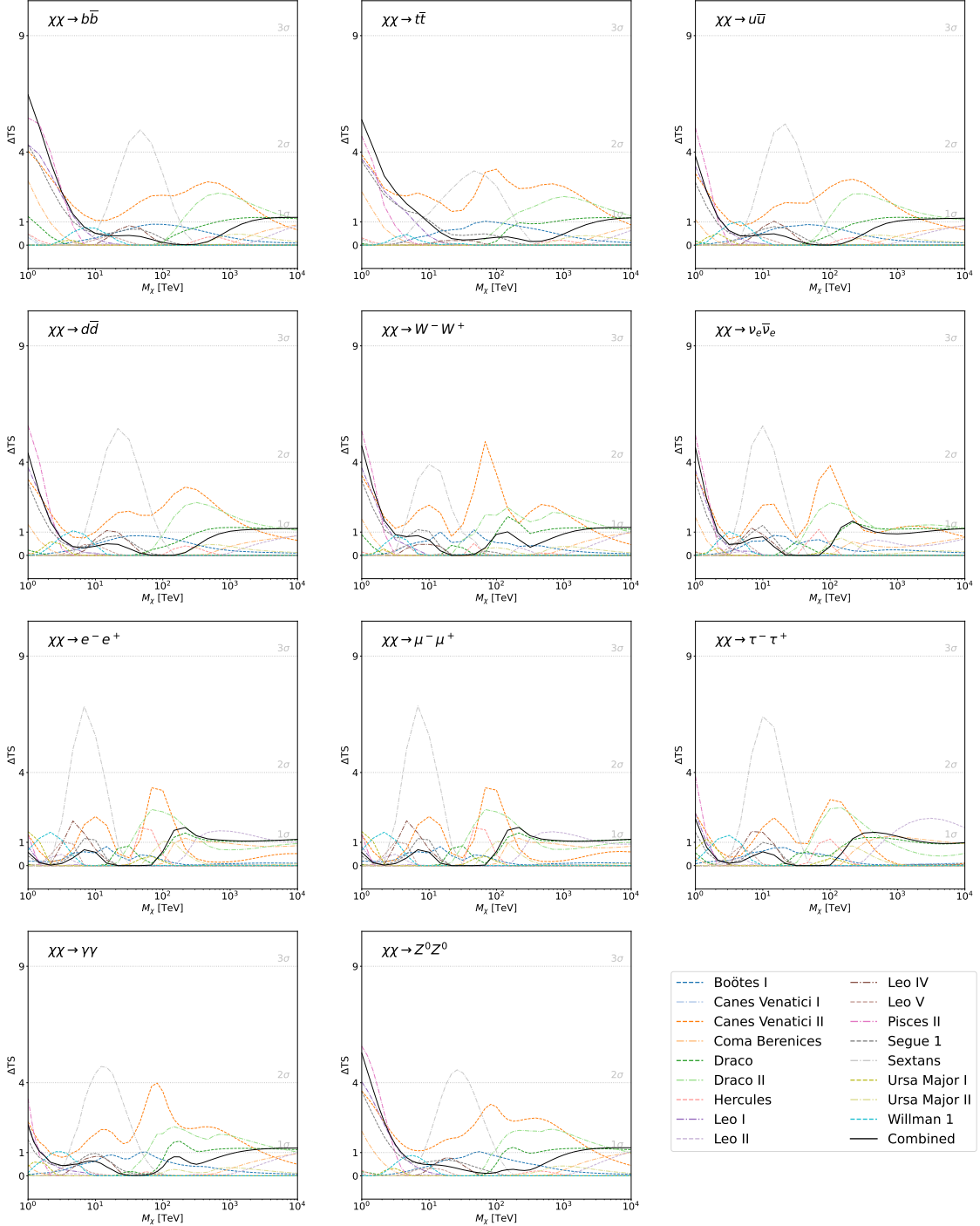


Figure 8. Same as Fig. 7 but with \mathcal{GS} J -factors.

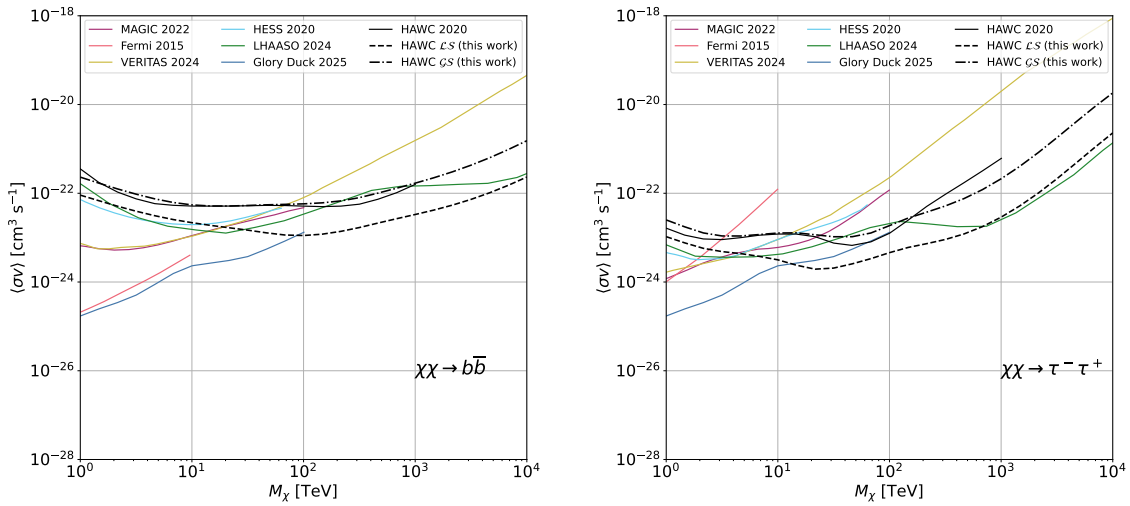


Figure 9. Comparison of HAWC combined limits using $\mathcal{L}\mathcal{S}$ and $\mathcal{G}\mathcal{S}$ J -factors to other DM searches for $b\bar{b}$ and $\tau^-\tau^+$. Each plot shows the 95% confidence limits using $\mathcal{L}\mathcal{S}$ and $\mathcal{G}\mathcal{S}$ J -factors in dashed and dash-dotted lines, respectively, a previous HAWC DM search [10] in the black solid line, and limits from other, similar DM searches (Fermi-LAT [24], Glory Duck (multi-experiment analysis) [9], H.E.S.S. [25], MAGIC [26], LHAASO [27], and VERITAS [28]) in colored solid lines.

dataset used here makes gamma-hadron separation cuts with the use of ML, which has strengthened our precision significantly [13]. Both tables are organized following HAWC’s binning scheme, defined in [15]. Each bin spans a quarter decade in log space across HAWC’s full energy sensitivity range. The 95% confidence limits on the flux assuming a power law with spectral index $\Gamma = -2$ are reported in Tab. 3.

6 Conclusion and Discussion

In this analysis, we have used observations of 17 dSphs from HAWC to perform a collective DM annihilation search towards dSphs. The data were combined across sources to increase the sensitivity of the search. Moreover, the current HAWC dataset yields significant improvement in sensitivity by means of more precise discrimination between cosmic and gamma rays. We have observed no significant deviation from the null hypothesis, and so present our results in terms of upper limits on the velocity-weighted cross-section, $\langle\sigma v\rangle$, for 11 potential DM annihilation channels across four decades of DM mass.

Source	316-562 GeV	562-1000 GeV	1.00-1.78 TeV	1.78-3.16 TeV	3.16-5.62 TeV	5.62-10.0 TeV	10.0-17.8 TeV	17.8-31.6 TeV	31.6-56.2 TeV	56.2-100 TeV	100-177 TeV	177-316 TeV
$\times 10^{-13} [\text{TeV}^{-1} \text{cm}^{-2} \text{s}^{-1}]$												
Boötes I	0 ⁺¹³ ₋₁₃	7.52 ^{+9.3} _{-7.5}	0.567 ^{+2.9} _{-0.57}	0.643 ^{+1.5} _{-0.64}	0.515 ^{+0.89} _{-0.52}	0 ^{+0.45} _{-0.41}	0.595 ^{+0.41} _{-0.41}	0.04 ^{+0.27} _{-0.04}	0.105 ^{+0.19} _{-0.1}	0 ^{+0.11} _{-0.1}	0 ^{+0.27} _{-0.27}	0 ^{+0.55} _{-0.55}
Canes Venatici I	26 ⁺⁴² ₋₂₆	4.02 ⁺¹⁹ ₋₄	0 ^{+1.1} _{-1.1}	0 ^{+1.5} _{-1.5}	0 ^{+0.53} _{-0.53}	0 ^{+0.16} _{-0.16}	0 ^{+0.21} _{-0.21}	0 ^{+0.11} _{-0.11}	0.0558 ^{+0.25} _{-0.56}	0.248 ^{+0.35} _{-0.25}	0 ^{+0.27} _{-0.27}	0.618 ^{+0.96} _{-0.62}
Canes Venatici II	45.5 ⁺³⁰ ₋₃₀	12.6 ⁺¹⁴ ₋₁₃	1.73 ^{+3.9} _{-1.7}	0 ^{+1.3} _{-1.3}	0.549 ^{+1.1} _{-0.55}	0.523 ^{+0.57} _{-0.52}	0 ^{+0.31} _{-0.31}	0 ^{+0.088} _{-0.088}	0.085 ^{+0.23} _{-0.85}	0.326 ^{+0.28} _{-0.28}	0 ^{+0.33} _{-0.33}	0 ^{+0.48} _{-0.48}
Coma Berenices	42.4 ⁺²¹ ₋₂₁	0 ^{+5.5} _{-5.5}	0.251 ^{+2.8} _{-2.5}	0 ^{+1.4} _{-1.4}	0.509 ^{+0.89} _{-0.91}	0 ^{+0.42} _{-0.42}	0 ^{+0.31} _{-0.31}	0 ^{+0.14} _{-0.14}	0 ^{+0.13} _{-0.13}	0 ^{+0.19} _{-0.19}	0.722 ^{+0.92} _{-0.72}	0 ^{+0.52} _{-0.52}
Draco	0 ⁺⁵⁵ ₋₅₅	0 ⁺³⁵ ₋₃₅	0 ^{+8.6} _{-8.6}	0 ^{+7.9} _{-7.9}	0 ^{+3.1} _{-3.1}	0 ^{+0.98} _{-0.98}	0.422 ^{+1.1} _{-0.42}	0.253 ^{+0.81} _{-0.25}	0 ^{+0.59} _{-0.59}	0 ^{+0.41} _{-0.41}	1.13 ^{+1.3} _{-1.3}	0 ^{+0.63} _{-0.63}
Draco II	0 ^{+7.7} _{-6.03}	0 ^{+9.3e+02} _{-9.3e+02}	0.174 ^{+7.5} _{-0.17}	0 ^{+2.2} _{-2.2}	0 ^{+2.6} _{-2.6}	0 ^{+1.1} _{-1.1}	0 ^{+0.5} _{-0.5}	0 ^{+0.95} _{-0.95}	0.291 ⁺¹ _{-0.29}	0 ^{+0.55} _{-0.55}	2.21 ^{+2.6} _{-2.2}	0 ^{+1.7} _{-1.7}
Hercules	30.1 ⁺²² ₋₂₂	0 ⁺² ₋₂	0 ^{+1.9} _{-1.9}	0 ^{+0.82} _{-0.82}	0 ^{+0.39} _{-0.39}	0.0404 ^{+0.48} _{-0.04}	0 ^{+0.16} _{-0.16}	0 ^{+0.17} _{-0.17}	0.474 ^{+0.32} _{-0.32}	0.0456 ^{+0.21} _{-0.06}	0 ^{+0.29} _{-0.29}	0 ^{+0.48} _{-0.48}
Leo I	44.8 ⁺²² ₋₂₂	15.8 ^{+9.7} _{-9.7}	0 ^{+1.9} _{-1.9}	0 ^{+1.3} _{-1.3}	0.252 ^{+0.86} _{-0.25}	0 ^{+0.26} _{-0.26}	0 ^{+0.26} _{-0.26}	0 ^{+0.11} _{-0.11}	0 ^{+0.11} _{-0.11}	0 ^{+0.11} _{-0.11}	0 ^{+0.29} _{-0.29}	0 ^{+0.52} _{-0.52}
Leo II	25.3 ⁺²⁰ ₋₂₀	0 ^{+6.2} _{-6.2}	2.97 ^{+2.8} _{-2.8}	1.88 ^{+1.4} _{-1.4}	0.175 ^{+0.81} _{-0.81}	0 ^{+0.22} _{-0.22}	0 ^{+0.18} _{-0.18}	0 ^{+0.2} _{-0.2}	0 ^{+0.098} _{-0.098}	0 ^{+0.088} _{-0.088}	0 ^{+0.32} _{-0.32}	0.778 ^{+0.99} _{-0.78}
Leo IV	0 ⁺¹⁰ ₋₁₀	0 ⁺¹⁶ ₋₁₆	0 ^{+1.8} _{-1.8}	2.63 ^{+2.5} _{-2.5}	2.7 ^{+1.4} _{-1.4}	0 ^{+0.6} _{-0.6}	0.292 ^{+0.5} _{-0.29}	0 ^{+0.18} _{-0.18}	0 ^{+0.26} _{-0.26}	0 ^{+0.16} _{-0.16}	0 ^{+0.73} _{-0.73}	0 ^{+0.57} _{-0.57}
Leo V	0 ⁺²⁸ ₋₂₈	0 ^{+9.2} _{-9.2}	3.78 ^{+4.6} _{-3.8}	1.29 ^{+2.2} _{-1.3}	1.55 ^{+1.2} _{-1.2}	0 ^{+0.18} _{-0.18}	0.117 ^{+0.41} _{-0.12}	0 ^{+0.04} _{-0.04}	0 ^{+0.18} _{-0.18}	0 ^{+0.095} _{-0.095}	0 ^{+0.33} _{-0.33}	0 ^{+0.55} _{-0.55}
Pisces II	47.8 ⁺²⁸ ₋₂₈	7.38 ⁺¹³ ₋₁₃	0.336 ^{+3.7} _{-0.34}	0 ^{+0.4} _{-0.4}	0 ^{+0.54} _{-0.54}	0.186 ^{+0.4} _{-0.19}	0 ^{+0.23} _{-0.23}	0 ^{+0.14} _{-0.14}	0 ^{+0.22} _{-0.22}	0 ^{+0.3} _{-0.3}	0 ^{+1.1} _{-1.1}	0 ^{+0.52} _{-0.52}
Segue 1	40.6 ⁺²⁰ ₋₂₀	7.39 ⁺⁹ _{-7.4}	0 ^{+2.7} _{-2.7}	0.443 ^{+1.4} _{-0.44}	0.41 ^{+0.8} _{-0.41}	0.437 ^{+0.49} _{-0.44}	0 ^{+0.17} _{-0.17}	0 ^{+0.088} _{-0.088}	0 ^{+0.12} _{-0.12}	0 ^{+0.3} _{-0.3}	0 ^{+0.53} _{-0.53}	
Sextans	76.3 ⁺⁵¹ ₋₅₁	0 ^{+4.3} _{-4.3}	0 ^{+2.3} _{-2.3}	0 ^{+1.9} _{-1.9}	2.74 ^{+1.5} _{-1.5}	0.88 ^{+0.78} _{-0.78}	0.512 ^{+0.51} _{-0.51}	0 ^{+0.31} _{-0.31}	0 ^{+0.21} _{-0.21}	0 ^{+0.22} _{-0.22}	0 ^{+0.33} _{-0.33}	0 ^{+0.56} _{-0.56}
Ursa Major I	0 ⁺¹⁴ ₋₁₄	51.3 ^{+1.2e+02} ₋₅₁	12.6 ⁺²⁰ ₋₁₃	2.77 ^{+6.7} _{-2.8}	0 ^{+1.1} _{-1.1}	0 ^{+0.26} _{-0.26}	0 ^{+0.26} _{-0.26}	0.758 ^{+0.69} _{-0.69}	0.181 ^{+0.44} _{-0.18}	0.0426 ^{+0.34} _{-0.033}	0 ^{+0.46} _{-0.46}	0.291 ^{+1.1} _{-0.29}
Ursa Major II	0 ^{+1.9e+03} _{-1.9e+02}	0 ^{+1.5e+02} _{-1.5e+02}	0 ⁺²⁰ ₋₂₀	0 ^{+4.6} _{-4.6}	0 ^{+8.1} _{-8.1}	0 ^{+1.6} _{-1.6}	0 ^{+0.71} _{-0.71}	0 ^{+0.31} _{-0.31}	0.365 ^{+0.95} _{-0.37}	3.37 ^{+1.9} _{-1.9}	1.07 ^{+1.8} _{-1.1}	0 ^{+1.2} _{-1.2}
Willman 1	0 ⁺¹⁶ ₋₁₆	168 ^{+1.1e+02} _{-1.1e+02}	0 ^{+6.8} _{-6.8}	6.41 ⁺⁶ ₋₆	1.04 ^{+2.9} ₋₁	0 ^{+0.9} _{-0.9}	0 ^{+0.24} _{-0.24}	0.476 ^{+0.67} _{-0.38}	0 ^{+0.18} _{-0.18}	0 ^{+0.22} _{-0.22}	0 ^{+0.33} _{-0.33}	0 ^{+0.73} _{-0.73}

Table 2. Gamma-ray flux best fit for each source assuming a power law with $\Gamma = -2$. Lower error was removed on flux points equal to zero.

Source	316-562 GeV	562-1000 GeV	1.00-1.78 TeV	1.78-3.16 TeV	3.16-5.62 TeV	5.62-10.0 TeV	10.0-17.8 TeV	17.8-31.6 TeV	31.6-56.2 TeV	56.2-100 TeV	100-177 TeV	177-316 TeV
	[$\log_{10}(\text{TeV}^{-1} \text{cm}^{-2} \text{s}^{-1})$]											
Bootes I	-11.89	-11.77	-12.46	-12.67	-12.87	-13.35	-13.00	-13.51	-13.53	-13.97	-13.56	-13.26
Canes Venatici I	-11.17	-11.64	-12.98	-12.82	-13.28	-13.80	-13.68	-13.96	-13.52	-13.22	-13.57	-12.80
Canes Venatici II	-11.12	-11.58	-12.25	-12.89	-12.81	-12.96	-13.51	-14.06	-13.50	-13.22	-13.48	-13.32
Coma Berenices	-11.20	-12.26	-12.51	-12.87	-12.87	-13.38	-13.51	-13.85	-13.88	-13.72	-12.81	-13.29
Draco	-11.26	-11.46	-12.07	-12.10	-12.51	-13.01	-12.82	-12.97	-13.23	-13.39	-12.61	-13.20
Draco II	-9.11	-10.03	-12.12	-12.66	-12.59	-12.97	-13.30	-13.02	-12.89	-13.26	-12.32	-12.76
Hercules	-11.29	-12.69	-12.71	-13.09	-13.41	-13.28	-13.80	-13.76	-13.10	-13.58	-13.53	-13.32
Leo I	-11.18	-11.59	-12.72	-12.90	-12.95	-13.59	-13.59	-13.95	-13.97	-13.95	-13.54	-13.29
Leo II	-11.34	-12.21	-12.24	-12.48	-13.01	-13.67	-13.74	-13.69	-14.01	-14.06	-13.49	-12.75
Leo IV	-11.99	-11.79	-12.75	-12.29	-12.39	-13.22	-13.10	-13.75	-13.59	-13.81	-13.13	-13.25
Leo V	-11.56	-12.03	-12.08	-12.46	-12.56	-13.73	-13.28	-14.03	-13.75	-14.02	-13.48	-13.26
Pisces II	-11.12	-11.70	-12.39	-13.40	-13.39	-13.27	-13.23	-13.64	-13.86	-13.67	-13.52	-12.95
Segne 1	-11.21	-11.79	-12.58	-12.72	-12.92	-13.04	-13.76	-14.06	-14.07	-13.91	-13.53	-13.27
Sextans	-10.90	-12.37	-12.63	-12.72	-12.38	-12.78	-12.99	-13.51	-13.68	-13.66	-13.48	-13.25
Ursa Major I	-11.86	-10.76	-11.49	-12.02	-12.97	-13.58	-13.59	-12.84	-13.21	-13.42	-13.34	-12.85
Ursa Major II	-9.71	-10.83	-11.70	-12.34	-12.09	-12.81	-13.15	-13.51	-12.88	-12.27	-12.54	-12.91
Willman 1	-11.79	-10.56	-12.17	-11.90	-12.41	-13.05	-13.61	-12.94	-13.73	-13.67	-13.48	-13.14

Table 3. 95% upper bounds on gamma flux for each bin and source assuming a power law with $\Gamma = -2$.

Finally, statistical studies with Poisson variation of HAWC’s background are essential to a comprehensive understanding of our observed excesses. We have seen that across both catalogs, the observed limits generally fall in line with the expectations. While in some channels at low masses we see the observed annihilation cross-section falling slightly above the 95% containment bands, these deviations correspond to significance well below 3σ . Thus, we observe no significant detection of WIMP dark matter with HAWC within our mass range and instead set limits on the annihilation cross-section. The $\mathcal{L}\mathcal{S}$ catalog sets some of the strongest current limits for WIMP DM annihilation from dSphs. The $\mathcal{G}\mathcal{S}$ catalog maintains similarly strong limits, especially for DM masses near 1 PeV.

Acknowledgments

We acknowledge the support from: the US National Science Foundation (NSF); the US Department of Energy Office of High-Energy Physics; the Laboratory Directed Research and Development (LDRD) program of Los Alamos National Laboratory; Consejo Nacional de Ciencia y Tecnología (CONACyT), México, grants LNC-2023-117, 271051, 232656, 260378, 179588, 254964, 258865, 243290, 132197, A1-S-46288, A1-S-22784, CF-2023-I-645, CBF2023-2024-1630, cátedras 873, 1563, 341, 323, Red HAWC, México; DGAPA-UNAM grants IG101323, IG100726, IN111716-3, IN111419, IA102019, IN106521, IN114924, IN110521, IN102223; VIEP-BUAP; PIFI 2012, 2013, PROFOCIE 2014, 2015; the University of Wisconsin Alumni Research Foundation; the Institute of Geophysics, Planetary Physics, and Signatures at Los Alamos National Laboratory; Polish Science Centre grant, 2024/53/B/ST9/02671; Coordinación de la Investigación Científica de la Universidad Michoacana; Royal Society - Newton Advanced Fellowship 180385; Gobierno de España and European Union-NextGenerationEU, grant CNS2023- 144099; The Program Management Unit for Human Resources & Institutional Development, Research and Innovation, NXPO (grant number B16F630069); Coordinación General Académica e Innovación (CGAI-UdeG), PRODEP-SEP UDG-CA-499; Institute of Cosmic Ray Research (ICRR), University of Tokyo. H.M. acknowledges support under grant number CBF2023-2024-1630. H.F. acknowledges support by NASA under award number 80GSFC21M0002. C.R. acknowledges support from National Research Foundation of Korea (RS-2023-00280210). We also acknowledge the significant contributions over many years of Stefan Westerhoff, Gaurang Yodh and Arnulfo Zepeda Domínguez, all deceased members of the HAWC collaboration. Thanks to Scott Delay, Luciano Díaz and Eduardo Murrieta for technical support.

References

- [1] G. Bertone and D. Hooper, *History of dark matter*, *Rev. Mod. Phys.* **90** (2018) 045002.
- [2] L.E. Strigari, *Galactic searches for dark matter*, *Physics Reports* **531** (2013) 1.
- [3] M.G. Baring, T. Ghosh, F.S. Queiroz and K. Sinha, *New limits on the dark matter lifetime from dwarf spheroidal galaxies using fermi-lat*, *Phys. Rev. D* **93** (2016) 103009.
- [4] HAWC collaboration, *The high-altitude water cherenkov (HAWC) observatory in México: The primary detector*, *Nuclear Instruments and Methods in Physics Research Section A: Accelerators, Spectrometers, Detectors and Associated Equipment* **1052** (2023) 168253.
- [5] A. Albert, R. Alfaro, C. Alvarez, J.D. Álvarez, R. Arceo, J.C. Arteaga-Velázquez et al., *Dark matter limits from dwarf spheroidal galaxies with the HAWC gamma-ray observatory*, *The Astrophysical Journal* **853** (2018) 154.

[6] A. Geringer-Sameth, S.M. Koushiappas and M. Walker, *Dwarf galaxy annihilation and decay emission profiles for dark matter experiments*, *The Astrophysical Journal* **801** (2015) 74.

[7] Pace, Andrew B and Strigari, Louis E, *Scaling relations for dark matter annihilation and decay profiles in dwarf spheroidal galaxies*, *Monthly Notices of the Royal Astronomical Society* **482** (2018) 3480.

[8] S. Ando, A. Geringer-Sameth, N. Hiroshima, S. Hoof, R. Trotta and M.G. Walker, *Structure formation models weaken limits on WIMP dark matter from dwarf spheroidal galaxies*, *Physical Review D* **102** (2020) .

[9] L. Collaboration, S. Abdollahi, L. Baldini, R. Bellazzini, B. Berenji, E. Bissaldi et al., *Combined dark matter search towards dwarf spheroidal galaxies with fermi-lat, hawc, h.e.s.s., magic, and veritas*, [2508.20229](#).

[10] A. Albert et al., *Search for gamma-ray spectral lines from dark matter annihilation in dwarf galaxies with the High-Altitude Water Cherenkov observatory*, *Phys. Rev. D* **101** (2020) 103001.

[11] A.U. Abeysekara et al., *Observation of the Crab Nebula with the HAWC gamma-ray observatory*, *The Astrophysical Journal* **843** (2017) 39.

[12] A. Albert, R. Alfaro, C. Alvarez, A. Andrés, J.C. Arteaga-Velázquez, D.A. Rojas et al., *Observation of the galactic center pевatron beyond 100 tev with hawc*, 2024.

[13] R. Alfaro, C. Alvarez, A. Andrés, E. Anita-Rangel, M. Araya, J.C. Arteaga-Velázquez et al., *Hawc performance enhanced by machine learning in gamma-hadron separation*, [2506.18277](#).

[14] J. Vikas and J.-B. Armelle, *HAWC high energy upgrade with a sparse outrigger array*, 2017. <https://doi.org/10.48550/arXiv.1708.04032>.

[15] HAWC collaboration, *Measurement of the Crab Nebula spectrum past 100 TeV with HAWC*, *The Astrophysical Journal* **881** (2019) 134.

[16] G. Vianello, R.J. Lauer, P. Younk, L. Tibaldo, J.M. Burgess, H. Ayala et al., *The multi-mission maximum likelihood framework (3ML)*, 2015. <https://doi.org/10.48550/arXiv.1507.08343>.

[17] HAWC collaboration, *Performance of the HAWC observatory and TeV gamma-ray measurements of the Crab Nebula with improved extensive air shower reconstruction algorithms*, *The Astrophysical Journal* **972** (2024) 144.

[18] C.W. Bauer, N.L. Rodd and B.R. Webber, *Dark matter spectra from the electroweak to the Planck scale*, *Journal of High Energy Physics* **2021** (2021) .

[19] M. Cirelli, G. Corcella, A. Hektor, G. Hütsi, M. Kadastik, P. Panci et al., *PPPC 4 DM ID: a poor particle physicist cookbook for dark matter indirect detection*, *Journal of Cosmology and Astroparticle Physics* **2011** (2011) 051.

[20] S. Miranelli, *Constraints on Lorentz-Invariance Violation with the HAWC Observatory*, Ph.D. thesis, Michigan State University, 2019.

[21] J.F. Navarro, C.S. Frenk and S.D.M. White, *The structure of cold dark matter halos*, *The Astrophysical Journal* **462** (1996) 563.

[22] A. Donath, R. Terrier, Q. Remy, A. Sinha, C. Nigro, F. Pintore et al., *Gammipy: A python package for gamma-ray astronomy*, *AandA* **678** (2023) A157.

[23] N. Evans, J. Sanders and A. Geringer-Sameth, *Simple J-factors and D-factors for indirect dark matter detection*, *Physical Review D* **93** (2016) .

[24] FERMI-LAT collaboration, *Searching for dark matter annihilation from Milky Way dwarf spheroidal galaxies with six years of Fermi Large Area Telescope data*, *Phys. Rev. Lett.* **115** (2015) 231301.

[25] H.E.S.S. collaboration, *Search for dark matter signals towards a selection of recently detected DES dwarf galaxy satellites of the milky way with H.E.S.S.*, *Phys. Rev. D* **102** (2020) 062001.

- [26] MAGIC collaboration, *Combined searches for dark matter in dwarf spheroidal galaxies observed with the MAGIC telescopes, including new data from coma berenices and draco*, *Physics of the Dark Universe* **35** (2022) 100912.
- [27] LHAASO collaboration, *Constraints on ultraheavy dark matter properties from dwarf spheroidal galaxies with LHAASO observations*, *Phys. Rev. Lett.* **133** (2024) 061001.
- [28] VERITAS collaboration, *An indirect search for dark matter with a combined analysis of dwarf spheroidal galaxies from VERITAS*, *Phys. Rev. D* **110** (2024) 063034.

A Likelihood Methods

The likelihood \mathcal{L} of each source for events that are Poisson distributed can be calculated as follows:

$$\mathcal{L} = \prod_i \frac{(B_i + S_i)^{N_i} e^{-(B_i + S_i)}}{N_i!}. \quad (\text{A.1})$$

Where B_i is the number of background counts observed, S_i is the sum of the expected number of signal counts, and N_i is the total number of counts. Both the background events B and the total number of counts N can be determined from HAWC's data. The excess of signal events S from DM-DM annihilation is determined by convolving Eq. (4.1) with HAWC's energy response and pixel point spread functions.

From here, the TS can be computed using the log-likelihood ratio test:

$$\text{TS}_{\max} = -2 \ln \left(\frac{\mathcal{L}_0}{\mathcal{L}^{\max}} \right). \quad (\text{A.2})$$

The null hypothesis likelihood \mathcal{L}_0 represents no DM detection and the best fit signal hypothesis \mathcal{L}^{\max} is where $\langle \sigma v \rangle$ maximizes the likelihood.

To determine the upper limit on $\langle \sigma v \rangle$ we define the parameter

$$\text{TS}_{95} \equiv \sum_{\text{bins}} \left[2N \ln \left(1 + \frac{\epsilon S_{\text{ref}}}{B} \right) - 2\epsilon S_{\text{ref}} \right]. \quad (\text{A.3})$$

Where S_{ref} is the expected number of excess counts in a bin for DM annihilation from a dwarf at the annihilation cross-section $\langle \sigma v \rangle$ and ϵ is a scaling factor. The 95% confidence level is then determined when

$$2.71 = \text{TS}_{\max} - \text{TS}_{95}. \quad (\text{A.4})$$

B Remaining Spectra Models

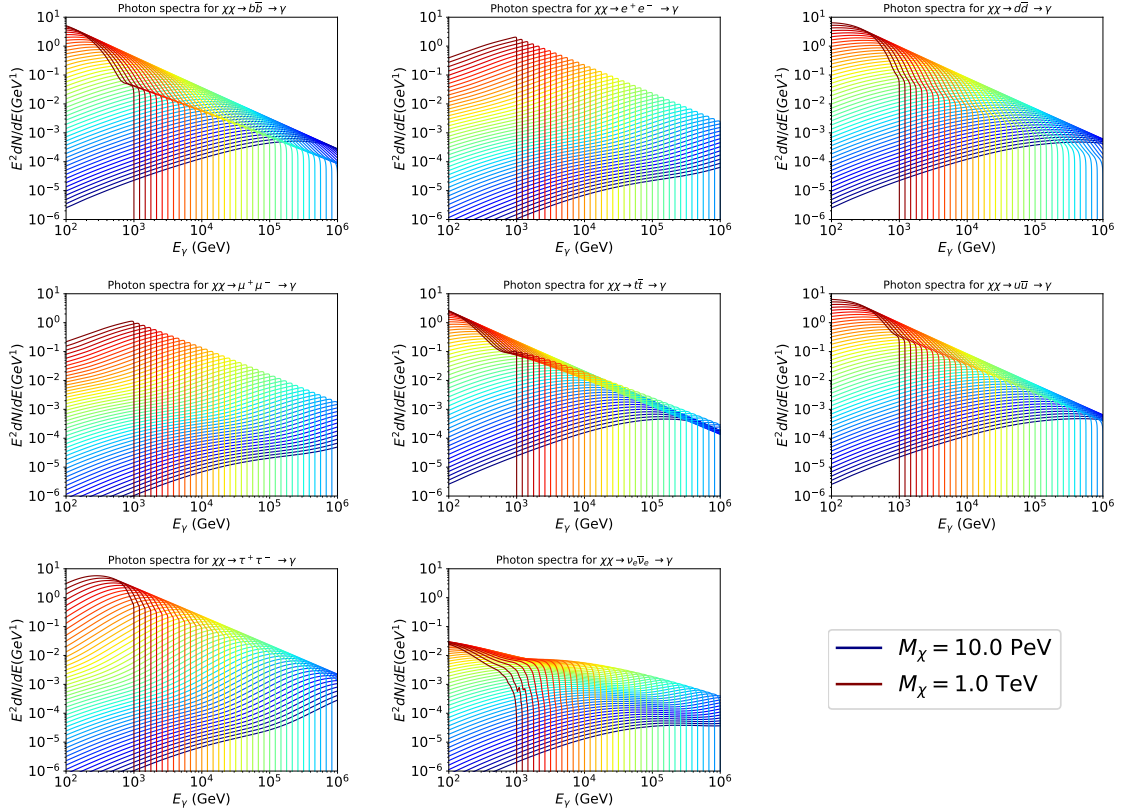


Figure 10. Spectral models for remaining SM channels. These did not require any additional smoothing and are directly pulled from [18]. Models that were manipulated further are in Sec. 4.1.

C Differential J -factor as a Function of θ

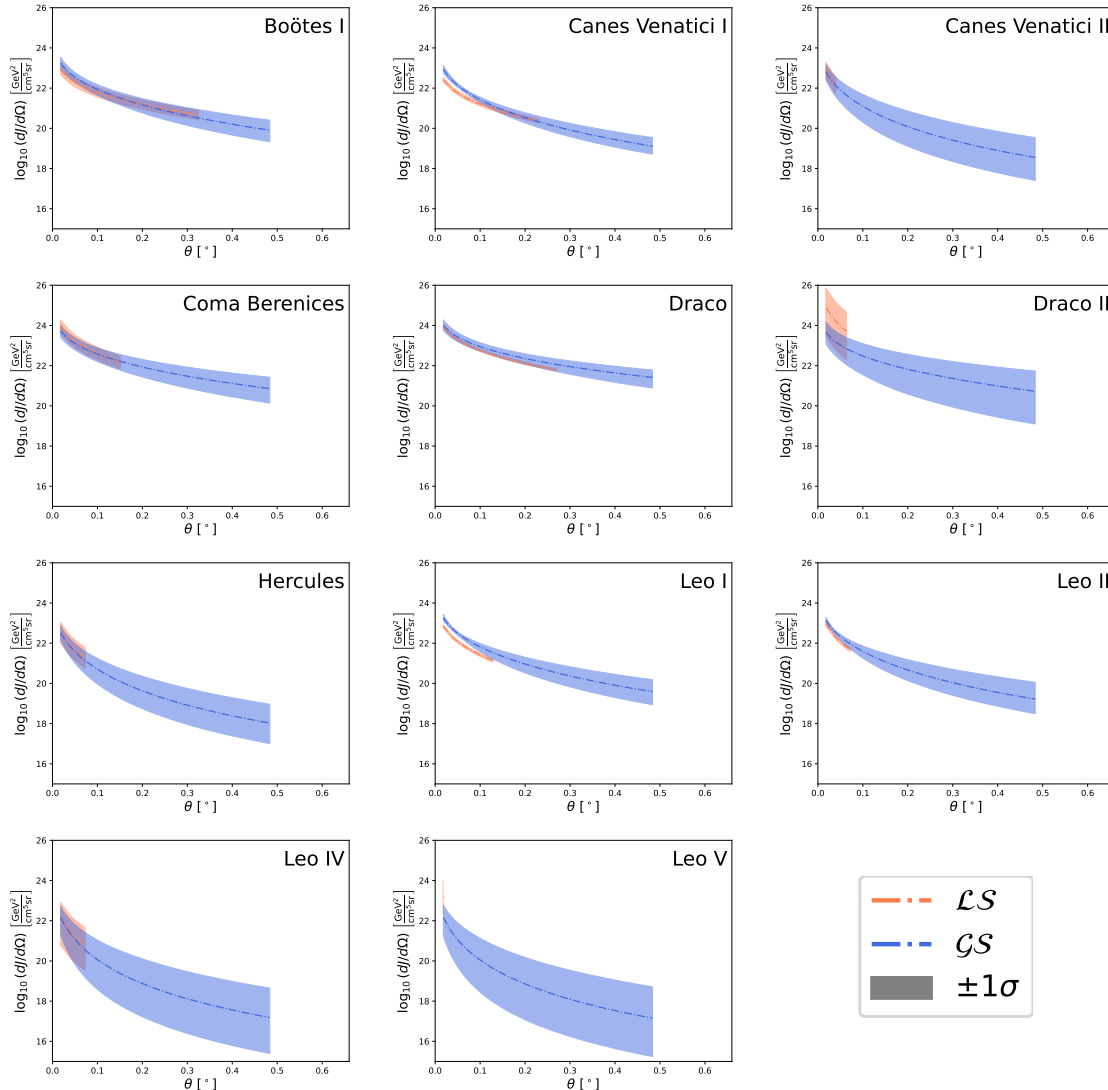


Figure 11. Differential J -factor as a function of θ for all dwarfs in both catalogs. The dashed orange and blue lines represents the median $\frac{dJ}{d\Omega}$ for the \mathcal{LS} and \mathcal{GS} catalogs. The shaded bands around each are the $\pm 1\sigma$ values. These are calculated from Gammapy’s Jfactory class for \mathcal{LS} where each distribution extends to a truncation radius, α_c , defined in Tab. 1, as determined in [8]. The Pisces II and Leo V distributions are not included here because they are treated as point sources due to their small truncation radius. For \mathcal{GS} , the uncertainty bands are calculated from 10,001 MC simulated parameters for \mathcal{GS} to a uniform radius of 0.5° , as defined in [7].

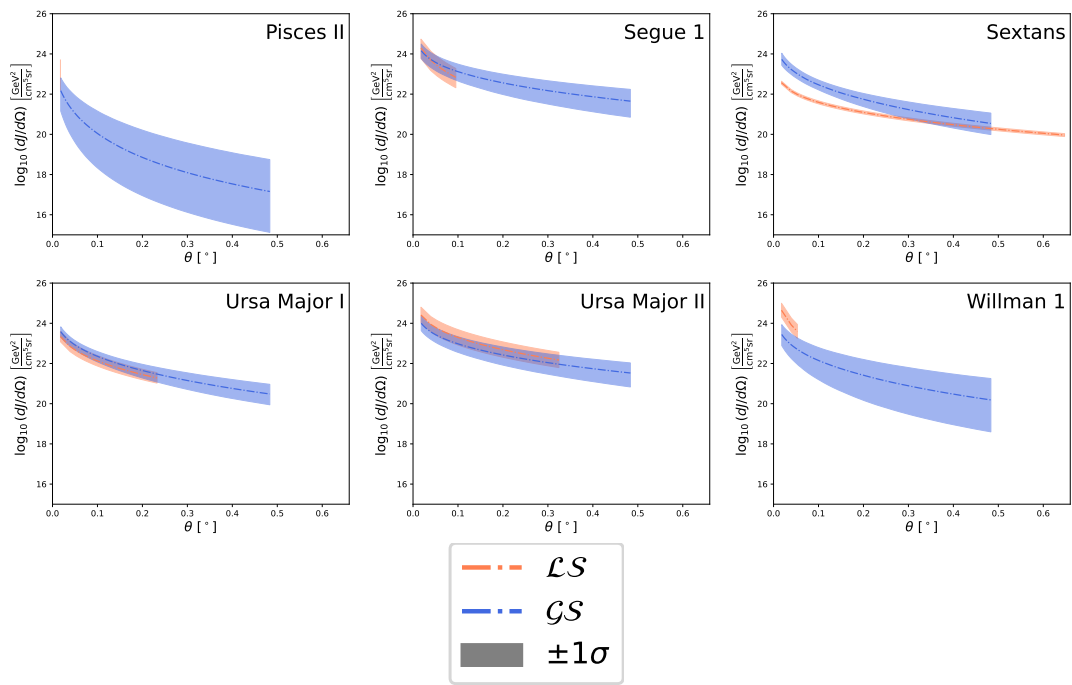


Figure 12. Continued from Fig. 11